Ranta, Janne; Polojärvi, Arttu

Limit mechanisms for ice loads on inclined structures: Local crushing

Published in:
Marine Structures

DOI:
10.1016/j.marstruc.2019.102633

Published: 31/05/2019

Document Version
Peer-reviewed accepted author manuscript, also known as Final accepted manuscript or Post-print

Please cite the original version:
Ranta, J., & Polojärvi, A. (2019). Limit mechanisms for ice loads on inclined structures: Local crushing. *Marine Structures*, *67*, Article 102633. https://doi.org/10.1016/j.marstruc.2019.102633

Limit Mechanisms for Ice Loads on Inclined Structures: Local Crushing

Janne Ranta, Arttu Polojärvi

Aalto University, School of Engineering, Department of Mechanical Engineering, P.O. Box 14300, FI-00076 Aalto, Finland

Sustainable Arctic Marine and Coastal Technology (SAMCoT), Centre for Research-based Innovation (CRI), Norwegian University of Science and Technology, Trondheim, Norway

---

Abstract

This paper focuses on mechanisms that limit the sea ice loads on offshore structures. It introduces a probabilistic limit load model, which can be used to analyze peak ice load events and to estimate the maximum peak ice load values on a wide, inclined, offshore structure. The model is based on simple mechanical principles, and it accounts for a mixed-mode ice failure process that includes buckling and local crushing of ice. The model development is based on observations on two-dimensional combined finite-discrete element method simulations on the ice-structure interaction process. The paper also presents a numerical limit load algorithm, which is an extension of the probabilistic limit load model and capable of yielding a large number of stochastic peak ice load values. The algorithm is compared to simulation-based and full-scale observations. Analyzing peak ice load events is challenging as sea ice goes through a complex mixed-mode failure process during such events. The algorithm is an effective tool for this analysis, and it shows that distinguishing between the buckling and local crushing failure is virtually impossible if the only data available from a peak load event is the value of the peak ice load. The algorithm shows potential in improving estimates of maximum peak ice load values on offshore structures.

Keywords: ice loads, offshore structures, Arctic engineering, ice-structure interaction, finite-discrete element method, discrete element method, ice mechanics

---

1. Introduction

Insight on sea ice behaviour and ice loads is important as it leads to safer and more sustainable Arctic operations, such as marine transportation, offshore wind energy, and offshore drilling. The ice loads arise from a complex and stochastic ice-structure interaction process, occurring as ice, moved by winds and currents, fails against an offshore structure [1–3] (Figure 1). It has become popular to develop rather complicated numerical tools to model ice actions, while the design of offshore structures still often relies on simplified ice load models and empirical load estimates. We believe the true value of the numerical models resides in careful analysis: It is the analysis that yields the insight on ice mechanics and ice loads. This insight makes it possible to conceive reliable, but simple enough, ice load models having the potential to improve the design of offshore structures.

This paper introduces a novel, but rather simple, approach for the analysis of maximum peak ice load events on a wide, inclined, offshore structure. The model development is based on hundreds of FEM-DEM-simulations [4, 5] and the introduced model extends our buckling model for peak ice loads [6]. Figure 1 shows snapshots from a simulation, in which an ice sheet moves against an inclined structure and fails into individual ice blocks and floes. These form an ice rubble pile in front of the structure. Figure 2 shows a maximum peak ice load event, in which the ice load is transmitted to the structure through a force chain [7, 8]. Here, the force chain is a series of ice blocks and floes under a high compressive load [9].

Our buckling model for ice loads assumed that the load on the structure is limited by the buckling of the force chain. This model accounted for the individual ice floes broken of the ice sheet and, as such, bears resemblance to some earlier models [10–12]. The model yielded the maximum peak ice load value (here and in the further text, superscript p refers to peak ice load) [6]

$$F^p = a\sqrt{kEI}, \tag{1}$$

where $a = a(\chi)$ is a buckling-mode-dependent dimensionless multiplier (Appendix A), $k = \rho_w g$ is the specific weight of water (here, ρ_w is the mass density of water and g the gravitational acceleration), E is the elastic modulus of ice, and $I = h^3/12$ is the second moment of area of a beam having a rectangular cross-section and thickness h (and unit width). The buckling model was used to analyze the strong effect of ice thickness h on the simulated peak ice load values [13]. This was done by first solving Equation 1 for a,

$$a = \frac{F^p}{\sqrt{kEI}}, \tag{2}$$

and then by showing that the hundreds of F^p values from the simulations led to a values, which did not show dependency on h. The buckling model was successful in quantifying the effect of h on the F^p values.

Though being successful in quantifying the effect of force chain buckling on F^p, the buckling model does not account for the compressive failure of ice: The model could theoretically allow F^p to increase above the compressive (or crushing) capacity of ice, which is physically not possible and calls for model improvement. The crushing strength of ice is often accounted for in studies on the relation between buckling and ice loads on vertical structures [1, 16–18], but its role in ice-inclined structure interaction is usually not accounted for or simply overlooked. The buckling model also does not fully account for the stochasticity of ice loads or the mixed-mode ice-structure interaction processes involving ice failure due to buckling and crushing [2, 3, 19]. Hendrikse and Metrikine [20] introduced a model for a mixed-mode ice failure process for vertical structures, but there is no comparable model for inclined structures. Earlier ice load models for inclined structures account in an approximate way for bending failure of ice, sliding and rotational motion of ice blocks, and the effect of ice rubble [21–24].

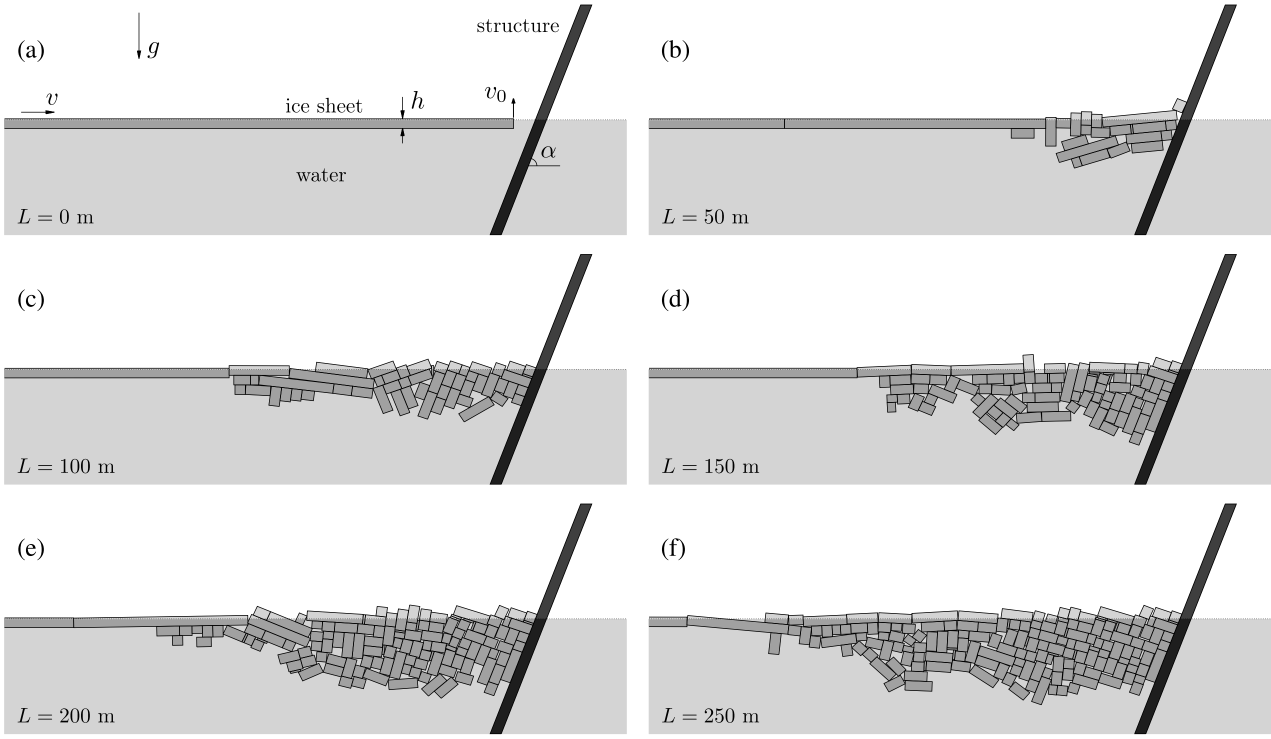

Figure 1: Snapshots of a 2D FEM-DEM-simulated ice-structure interaction process at six stages, each described by the length L of the ice pushed against an inclined structure. The ice sheet, moving at a constant velocity v, breaks into ice blocks, or floes, in the vicinity of the structure. Broken ice forms an ice rubble pile in front of the structure and transmits the load from the still-intact ice sheet to the structure. The first figure shows the initial vertical velocity perturbation v_0, which was used to vary initial conditions as decribed in Ranta [13]. Here the ice sheet thickness h was 1.25 m. The figure is reproduced from Ranta et al. [6].

The core contribution of this paper is in extending the buckling load model proposed by Ranta et al. [6] into a probabilistic limit load model, and further, into a numerical limit load algorithm. The model yields the probability for a peak ice load value in an ice-structure interaction process being limited by the buckling or local crushing failure of ice. It can also be used to study how these probabilities change with ice parameters and the geometry of the force chains. The ice parameters studied in this paper are the ice thickness and the crushing strength of ice. The numerical limit load algorithm extends the model into a tool for producing virtual ice load observations and estimates of ice loads. In addition to the mixed-mode failure, readily accounted for by the limit load model, the numerical algorithm accounts for the inherent stochasticity of the ice loads in an ice-structure interaction process. The algorithm attributes the stochasticity to the geometry of the force chains. We compare the results yielded by the algorithm against our simulations and validate them against full-scale data as presented by Timco and Johnston [25]. The algorithm demonstrates the challenges related to the thorough analysis of an ice-structure interaction process: We show that distinguishing between the buckling and local crushing failure in an ice load event is virtually impossible if the only data available from the peak load events are the values of the ice loads. As the data in this work is based on 2D simulations where grounding is not accounted for, the results of the model should apply to wide structures in deep waters.

Our paper first describes the FEM-DEM simulations and the probabilistic limit load model. Then the results related to the buckling model are reviewed and combined with the limit load model. After

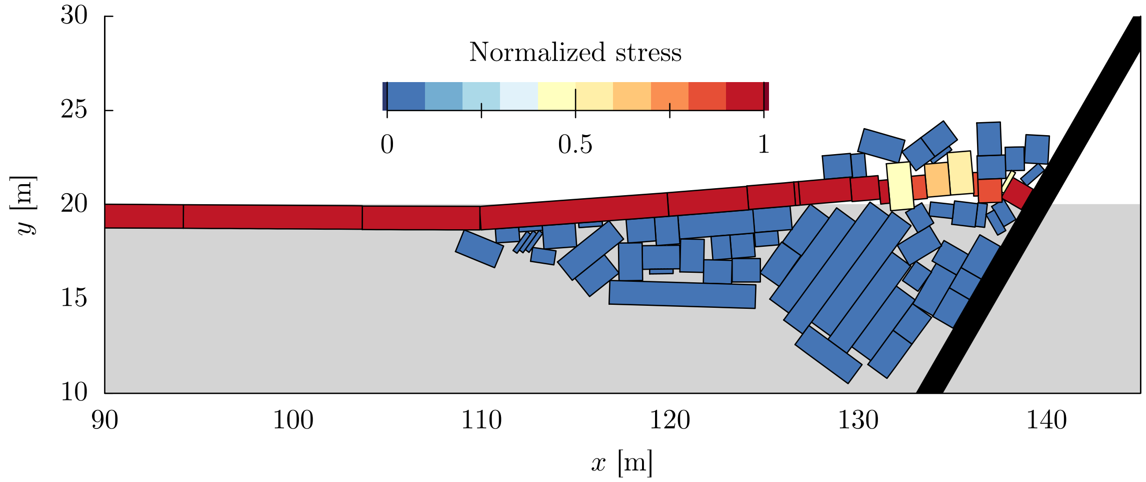

Figure 2: Snapshot from a FEM-DEM simulation showing a force chain — a sequence of ice blocks in contact due to high compressive stress — transmitting the load from the intact ice sheet, moving from the left towards an inclined structure. Colors indicate the average normalized compressive stress on the ice blocks. The stress measure is the so-called particle stress, describing the average compression of an ice block [7, 14, 15]. Here the ice sheet thickness h was 1.25 m.

this, the paper focuses on extending the limit load model into a numerical limit load algorithm and on the use of this algorithm in the analysis of the ice-structure interaction process. The algorithm is also verified against the limit load model, compared to the FEM-DEM simulations, and validated against full-scale observations. Before concluding the paper, we make some remarks on the applicability of the limit load model and algorithm.

2. Methods

2.1. Simulations of ice-structure process

The study is based on the combined finite-discrete element method (FEM-DEM) simulations [4, 26]. The simulations were performed with the 2D FEM-DEM code of the Aalto University Ice Mechanics Group [9, 27–29]. Paavilainen et al. [27, 28] found the model results to be in fair agreement with the laboratory and full-scale measurements by Saarinen [30] and the data reported in Timco and Johnston [25], respectively. The strength of FEM-DEM in ice mechanics resides in its ability to account for numerous individual ice floes and blocks and for the granular behavior of ice rubble. Models accounting for these features have been used in several studies on ice mechanics [31–49].

Figures 1a-f describe simulations that had an ice sheet of thickness h pushed against an inclined rigid structure. Approximately 100 m from the structure, a viscous damping boundary condition and a constant horizontal velocity $v = 0.05$ m/s were applied to the ice sheet. About 100 meters away from the structure, a viscous damping boundary condition was applied on the ice sheet to mimic a semi-infinite ice sheet being pushed against the structure [28]. This boundary condition may not be ideal for a case of a structure interacting with, for example, a floe field. Paavilainen et al. [27, 28] describe the model in detail. The sheet consists of rectangular discrete elements connected by viscous-elastic Timoshenko beams, which failed at locations where the beams met a pre-defined failure criterion proposed by Schreyer et al. [50]. The beams went through a cohesive softening process upon failure [51], with the energy dissipated due to this process matching that of the fracture energy of ice [52]. Table 1 gives the main parameters of the simulations.

Contact forces were solved using an elastic-viscous-plastic normal contact force model, together with an incremental tangential contact force model with Coulomb friction [27, 33]. The model describes local crushing at ice-block-to-ice-block and ice-structure contacts. The amount of local crushing was governed by the plastic limit parameter, σ_p, which relates the maximum contact load to the contact geometry. Plastic limit parameter σ_p accounts for the compressive strength of ice, or in other words, the local crushing between the contacting ice blocks. The maximum compressive force transmitted in a contact is the product of σ_p and the length of the contact (in 3D this would be the contact area). Hopkins [33] discusses the role of σ_p in detail. No new ice features were created, nor did the block geometries change during the local crushing (the model cannot be used to describe the continuous crushing of an intact ice sheet). Water was accounted for by applying a buoyant force and simplified drag model. The model is 2D and does not allow for clearing of the ice around the structure; thus, its results do not apply for slender structures.

The study is based on seven sets of simulations, S1...S7, summarized in Table 2. Each set contained 50 simulations, where all parameters, except the initial vertical velocity perturbation v_0, were constant. The initial velocity v_0 was of the order of 10^{-12} m/s at the free edge of the ice sheet (Figure 1a) and had a unique value for each simulation in a set. While the simulated processes themselves are deterministic, they are sensitive to initial conditions [54]: A small perturbation in the initial conditions of two simulations with the same parameterization is enough to lead to two different ice loading processes. Figure 3a demonstrates this by showing the ice load F measured on the structure as a function of the length L of the pushed ice sheet. The F-records are from two simulations of set S5, and they show very similar features. However, they diverge after $L = 10 \ldots 15$ m, and thus produce ice load data from two different ice loading processes. As shown in Table 2, the simulation sets S1...S6 differed from each other by the values of h and σ_p. Simulation set S7 had thick ice, $h = 1.25$ m, and a high value of 8 MPa for σ_p. The simulation sets allowed stochastic peak ice load events to be studied with full control of the parameters [6, 13, 54–56]. Often, studies on the statistics of ice loads are made based on full-scale data, on ice loads on ships and on fixed structures [3, 25, 57–65], in which case, such control is not possible.

Figures 3a and b illustrate the maximum peak load F^p events for two simulations. Since the F-records were different for all simulations, the F^p events in them occurred at a different time and yielded a different F^p value. As the close-ups in Figure 3b illustrate, the ice sheet typically advanced a few meters (up to tens of meters) during an F^p event; the events were not due to sudden impact loads. We recorded the maximum peak load F^p value from each simulation, as the F^p events and the resulting peak load values are usually of primary interest in Arctic engineering and in studies of ice loads. Often, they are the only result reported in the experiments.

Table 1: Summary of the main simulation parameters. Only the ice thickness h and the plastic limit σ_p were varied between simulation sets S1. . .S8 (Table 2 describes the simulations sets). The parameter values were mostly chosen following Timco and Weeks [53]. Fracture energy was chosen after Dempsey et al. [52].

	Description and symbol		Unit	Value
General	Gravitational acceleration	g	m/s^2	9.81
	Ice sheet velocity	v	m/s	0.05
	Drag coefficient			2.0
	Duration of the simulation		s	5000
	Total length of pushed ice		m	250
Ice	Thickness	h	m	0.5, 0.875, 1.25
	Elastic modulus	E	GPa	4
	Poisson's ratio			0.3
	Density		kg/m^3	900
	Tensile strength		MPa	0.6
	Shear strength		MPa	0.6
	Fracture energy		J/m^2	12
Contact	Plastic limit	σ_p	MPa	1.0, 2.0, 8.0
	Ice-ice friction coefficient			0.1
	Ice-structure friction coefficient			0.1
Water	Density	ρ_w	kg/m^3	1010
Structure	Slope angle		deg	70

Table 2: Simulation sets S1. . .S7 of this study. The table also shows the number N and the indices (ID) of the simulations in each set. Detailed list of simulation parameters is given in Table 1.

Set	ID	N	h	σ_p
			[m]	[MPa]
S1	1-50	50	0.5	1
S2	51-100	50	0.5	2
S3	101-150	50	0.875	1
S4	151-200	50	0.875	2
S5	201-250	50	1.25	1
S6	251-300	50	1.25	2
S7	301-350	50	1.25	8

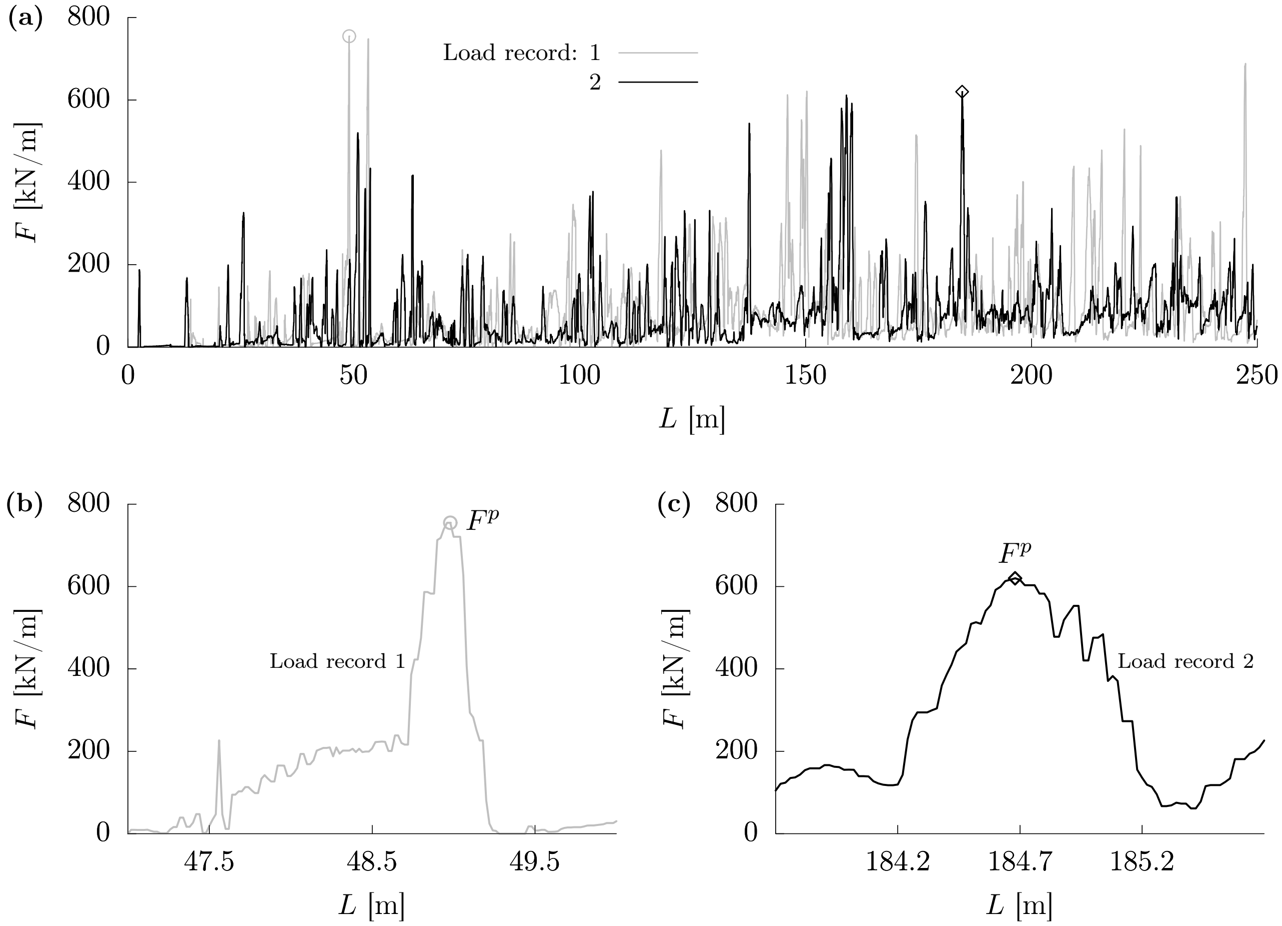

Figure 3: Examples of ice load F records yielded by our simulations: (a) shows two F-records plotted against length L of pushed ice and (b) close-ups of the maximum peak ice load F^p events from the same two simulations. On a general level, the F-records consist of consecutive peak load events, of which one corresponds to the maximum peak load F^p. Here the ice thickness $h = 1.25$ m and the plastic limit $\sigma_p = 1$ MPa in both simulations, which only differed by the value of the initial velocity perturbation v_0 (Figure 1).

2.2. Probabilistic limit load model

The probabilistic limit load model assumes that the peak ice loads are related to the force chains, which transmit the load from the intact ice sheet to the structure (Figure 2). The model uses the above-described buckling model [6], which is extended into the probabilistic limit load model by (1) supplementing it with a local crushing model and (2) by accounting for the stochasticity in the contact geometries of the blocks belonging to the force chains. The model estimates maximum peak ice load during an ice-structure interaction process. These usually occur after the initial stages of the process and the model does not consider parameters, such as the inclination angle of the structure, which may strongly affect the loads in the beginning of the process, but only weakly later into it [1, 13, 56].

An elementary unit of the model, shown in Figure 4, is a contact interface between a pair of ice blocks belonging to a force chain. The blocks are in partial face-to-face contact due to a compressive load P, which the force chain transmits. The crushing model assumes that local crushing occurs at the interface of the two blocks if $P \geq \bar{h}\sigma_p$, where $\bar{h}$ is the length of the contact interface and σ_p is the limit for compressive stress (also the blocks are assumed to have a unit width). For simplicity, the line of action for P in Figure 4 is assumed to remain on a straight line, and the model remains unchanged

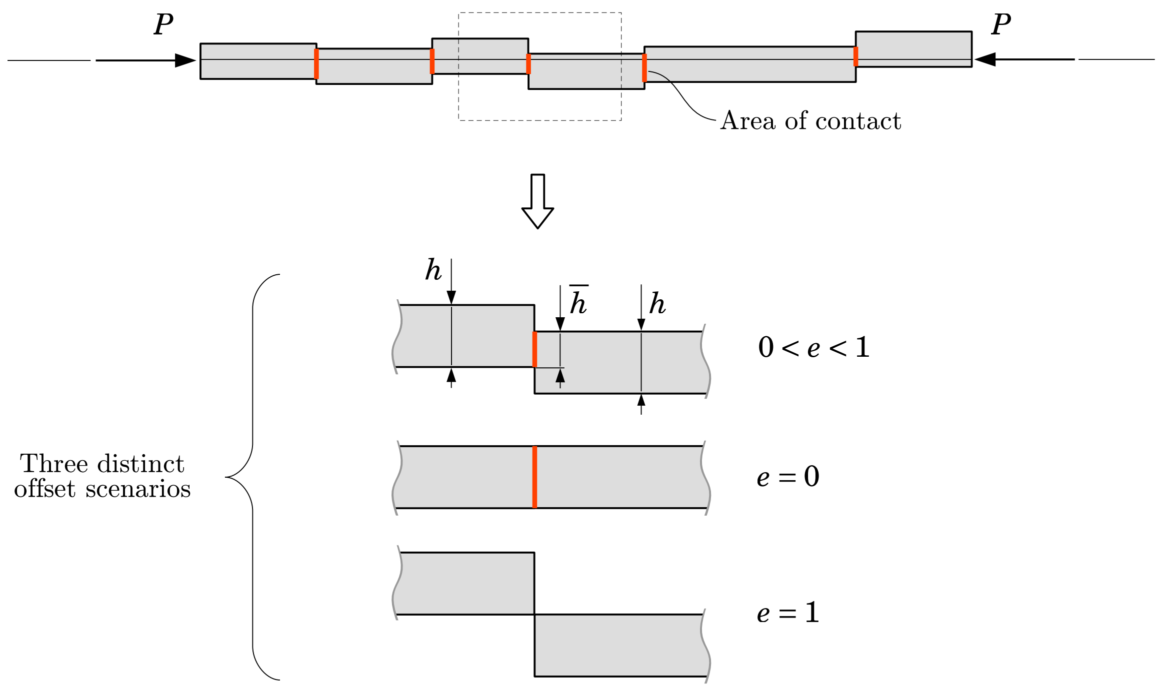

Figure 4: An illustration of a force chain transmitting a load P and a contact interface between a pair of ice blocks having a contact length of $\bar{h}$. The figure also shows three different contact offset scenarios, each having a different non-dimensional offset, $e = 1 - \bar{h}/h$, where h is the ice thickness.

for curved force chains (Figure 2), for which P can be assumed to be approximately constant along the length of the chain.

By using Equation 1 and the criterion $P \geq \bar{h}\sigma_p$ for local crushing, it is simple to determine the critical contact length $\bar{h}_c$, for which the local crushing event occurs with the same compressive load as the buckling. The critical contact length is the limit where the cause of failure for a pair of blocks changes from buckling to local crushing, and it is obtained via the following

$$\sigma_p \bar{h}_c = a\sqrt{kEI} \quad \Rightarrow \quad \bar{h}_c = \frac{a}{\sigma_p}\sqrt{kEI} = \frac{a}{\sigma_p}\sqrt{\frac{\rho_w g E h^3}{12}}. \tag{3}$$

When the contact length $\bar{h} \leq \bar{h}_c$ for a given pair of contacting blocks, then the local crushing event limits the P transmitted by them. In contrast, when $\bar{h} > \bar{h}_c$, buckling limits P. We would like to emphasize that the model accounts for the root cause of failure only, and it assumes that the load P is limited by failure due to either buckling or local crushing. The two failure modes are assumed to not occur simultaneously, but, for example, the blocks of the force chain could buckle immediately after the initial failure by local crushing.

When including stochasticity in the model, the contact length $\bar{h}$ and ice thickness h are used to introduce a non-dimensional contact offset (Figure 4)

$$e = 1 - \frac{\bar{h}}{h}, \tag{4}$$

where, by definition, $0 \leq e \leq 1$. The critical contact offset e_c, at which the load-limiting mechanism changes from buckling to local crushing, is achieved by substituting $\bar{h}_c$ into the previous equation:

$$e_c = 1 - \frac{\bar{h}_c}{h} = 1 - \frac{a\sqrt{kEI}}{\sigma_p h} = 1 - \frac{a}{\sigma_p}\sqrt{\frac{\rho_w g E h}{12}}. \tag{5}$$

The above equations, together with Equation 1 and an assumption of a being independent of e, can be used to write the maximum load P^m, which a system with one contact interface is able to transmit as

$$P^m = \begin{cases} a\sqrt{kEI} & \text{if } e < e_c \quad \text{(limiting mechanism: buckling)} \\ \sigma_p h(1-e) & \text{if } e \geq e_c. \quad \text{(limiting mechanism: local crushing).} \end{cases} \tag{6}$$

This equation is applicable for a pair of blocks in all force chain-induced peak load events in an ice-structure interaction process (Figure 3). In other words, it is not restricted to modeling the maximum peak ice load event only.

In a peak load event that occurs during an ice-structure interaction process, the e values for the pairs of contacting blocks in force chains vary randomly. To use the model for predicting the limiting mechanism in *the maximum peak ice load event only*, the model requires e to have a reasonable maximum contact offset length, e_m. Clearly, as Equation 4 and Figure 4 demonstrate, e could vary between values of 0 and 1. When $e = 0$, the contact length $\bar{h}$ is equal to the ice thickness h. When $e = 1$, the contact length becomes zero and the force chain does not exist. Thus, for a given pair of adjacent blocks in a force chain, e can have a random value varying at an interval of $0 \ldots e_m$, where $0 < e_m < 1$. The distribution for e values is not known; thus, a simple triangular distribution that has its maximum at e_m was chosen here. This distribution (Figure 5a) has a cumulative distribution function (CDF)

$$T(e) = \begin{cases} 0 & , e < 0 \\ (2e_m - e)e/e_m^2 & , 0 \leq e \leq e_m \\ 1 & , e > e_m. \end{cases}, \quad \text{where} \quad 0 < e_m < 1 \tag{7}$$

Figures 5a-d illustrate the shape of $T(e)$, and the corresponding probability density function, $T_{\text{pdf}}(e)$, if one of the values, 0.6, 0.8 or 1.0, is chosen for e_m. The figures also show the cumulative and probability density functions for a more complicated normal distribution. The difference between the distributions is small and the simple triangular one is used here. It is important to notice that relating the randomness of the process to parameter e causes the stochasticity of the loads to be related to the geometrical configuration of the rubble pile. The configuration, on the other hand, can be justifiably considered to be a random physical property of the studied system consisting of still intact ice, ice rubble, and an inclined structure. Here the triangular distribution for e was chosen due to its simplicity, but as will be discussed below, other distributions for it should be tested in the future.

The choice of a triangular cumulative distribution function $T(e)$ leads to fairly simple formulas for the probabilities of buckling and local crushing events. In a system with one pair of contacting blocks and one contact interface, the buckling event limits the load when $e < e_c$. The probability of a buckling event is given by

$$p(\text{buckles}) = T(e_c) = 1 - \frac{1}{e_m^2}\left[e_m - 1 + \frac{a}{\sigma_p}\sqrt{\frac{\rho_w g E h}{12}}\right]^2, \quad 0 \leq e_c \leq e_m \quad \& \quad 0 \leq e_m < 1. \tag{8}$$

If the buckling event does not limit the load, then the local crushing event will limit it. The probability that the local crushing event in one contact interface limits the load is, thus, given by the complementary probability of the previous equation:

$$p(\text{crushes}) = 1 - p(\text{buckles}). \tag{9}$$

The final step in developing the model is to extend it so that it considers a force chain having n contact interfaces. For this step, it is assumed that the limit for the load is reached when the system buckles or when any of the contact interfaces locally crushes. If the conditions in all n contact interfaces are independent of each other, and such that the system will not undergo local crushing, the probability for buckling is

$$p_n(\text{buckles}) = \prod_{i=1}^{n} p(\text{buckles}) = p(\text{buckles})^n. \tag{10}$$

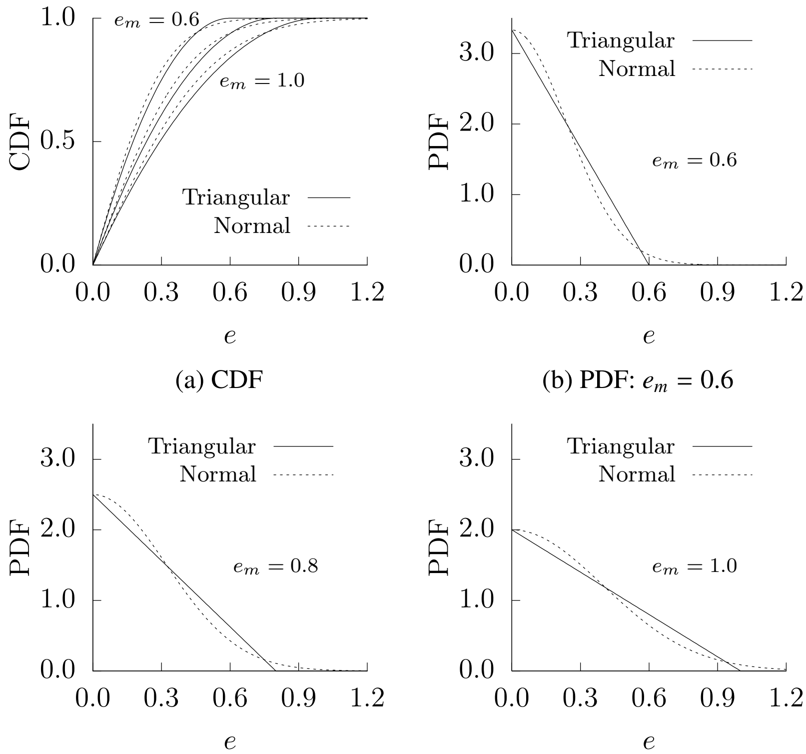

(a) CDF (b) PDF: $e_m = 0.6$

(c) PDF: $e_m = 0.8$ (c) PDF: $e_m = 1.0$

Figure 5: Functions describing the random non-dimensional offset e defined in Figure 4: (a) the cumulative distribution function $T(e)$ defined by Equation 7 and (b)-(d) the probability density functions (PDF) of a triangular distribution with $e_m = 0.6$, 0.8, and 1.0, respectively. For comparison, the figures also show corresponding functions derived using a standard normal distribution.

Again, the probability that a crushing event will limit the load is given by a complementary probability of the previous equation:

$$p_n(\text{crushes}) = 1 - p_n(\text{buckles}). \tag{11}$$

A simple way to demonstrate how the model works, and the parameter effects it yields, is to consider a hypothetical peak load event that a pair of blocks would cause if a triangular distribution with $e_m = 1$ were used (we emphasize that $e_\mathrm{m} = 1$ would allow the model to predict a zero maximum peak ice load value for an ice-structure interaction process). In this hypothetical case, the probability of a buckling event is

$$p_n(\text{buckles}) = \left[1 - \frac{a^2 \rho_w g E h}{12\sigma_p^2}\right]^n. \tag{12}$$

This example shows the following expected outcome. Force chains formed by ice blocks, that originate from an ice sheet with low E and/or h, are more prone to buckle than chains with blocks originating from a sheet with high E and/or h. This shows that the model yields plausible results: The buckling events are more likely to occur in the ice-structure interaction process when the ice is thin [1]. It is also justified to expect that an increase in the plastic limit σ_p makes a buckling event more likely to occur than a local crushing event. The previous equation shows that this, as well, is a result shown by the model.

3. Results

This section first reviews some of the results from Ranta et al. [6] and then uses them as input for the limit load model, which sheds light on the roles of buckling and local crushing in limiting the maximum peak ice load values.

3.1. Peak ice loads and buckling

Figure 6a shows the maximum peak ice load F^p values (Figure 3a and b) from our FEM-DEM simulations. Additionally, it shows the mean F^p values with their standard deviations for the simulations of each set, S1. . . S7 (Table 2). While the F^p values from the simulations in a given set show scatter, the mean F^p values of the sets S1. . . S7 differed considerably, by up to about 500 %, mainly due to a difference in ice thickness h between the sets[13]. The simulations with high σ_p in S7 yielded larger values than sets S5 and S6 with the same ice thickness, h = 1.25 m, but smaller σ_p. The variation between the F^p values yielded by the simulations in each set was largely due to the stochasticity of the ice loading process [13, 54, 55].

The values of a (Equation 2), solved using the F^p data in Figure 6a, are shown in Figure 6b and indicate that the peak load events were related to buckling. All of the mean a values are in the same range. There is no dependency between a and h. The mean a value is clearly larger in set S7, which had a high value for the plastic limit σ_p. However, the F^p values are well normalized by factor $\sqrt{kEI}$ (Equation 2), suggesting that buckling has an important role in limiting the peak ice load values. In other words, multiplying F^p by $1/\sqrt{h^3}$ yields normalized a data. Nonetheless, the data still shows scatter not explained by the buckling model.

Below, we will use the a values for the probabilistic limit load model, in which they only relate to the ice failure due to buckling (Equation 6). For finding a suitable a value for the limit load model, it is thus natural to look for a distribution for a using the simulation results, whereby local ice crushing would least likely affect the results. Figure 7a shows a histogram for the peak load F^p observations for set S7, which had a very high value of 8 MPa for σ_p — the simulations in S7 can be assumed to give F^p values governed by buckling and, thus, being virtually independent of local crushing. The figure also shows, and specifies, a two-parameter Gumbel (type I) extreme value distribution fitted to the a data (our previous study showed a values are likely Gumbel distributed [55]). Figure 7b shows the data quantiles from the same data plotted against Gumbel theoretical quantiles, with the linearity of the data points showing that the Gumbel distribution describes the data well.

3.2. Load limits due to buckling and crushing events

Figures 8a-d demonstrate the use of the probabilistic limit load model by showing the probabilities p_n(buckles) and p_n(crushes) of buckling or local crushing failure (Equations 10 and 11), respectively, limiting the peak ice load F^p value. While Figures 8a and b show p_n(buckles) and p_n(crushes) as a function of h, with σ_p fixed to 1 MPa, Figures 8c and d show them plotted against σ_p, with h fixed to 1.25 m. All figures show the results for the number n of ice floe contact interfaces 4 and 8. Figures 8a and b (and similarly c and d) differ by the value of e_m, which was 0.6 and 0.8, respectively. Parameter a was fixed to 0.39 corresponding with the mean a value for simulation set S7 (Figure 8b), while the other parameters were from Table 1.

Figures 8a-d show that the probabilistic limit load model yields some fairly intuitive, but also more surprising, results. The probability p_n(buckles) increases with σ_p and decreases with an increasing h. The first result is due to a high σ_p inhibiting the local crushing, while the latter can be understood by accounting for the buckling load being dependent on h (Equation 1 shows that the buckling load is proportional to $\sqrt{h^3}$). In addition, the figures show that the p_n(buckles) for fixed h or σ_p decreases when the number of contact interfaces, n, within the force chains increases. This underlines the importance of understanding local phenomena at the contact interfaces; the effect of local crushing may override the larger scale phenomena of force chain buckling, which is easier to detect. Figures 8a and b also show that for a fixed σ_p, n has no effect on the limit for h, at which peak loads become solely governed by buckling. This is shown by the p_n(crushing) being zero with $h \lessapprox 0.4$ m, when $\sigma_p = 2$ MPa ($h \lessapprox 0.1$ m, when $\sigma_p = 1$ MPa), for both values of n shown in the figure.

Figures 8c and d show an important outcome of the model. For a fixed h, soft ice (low σ_p) will never fail by buckling. For example, in the case of the figures where $h = 1.25$ m, the p_n(buckles) $= 0$ for $\sigma_p \lessapprox 1$ MPa. This means that soft ice will never exhibit any failure mode other than local crushing and that, consequently, (1) the mechanical phenomena limiting F^p values in ice-structure interaction differ drastically for soft and strong ice and (2) the analysis of ice loading processes should account for this fact. With respect to our discussion on this phenomenon in Section 4.4, we already note

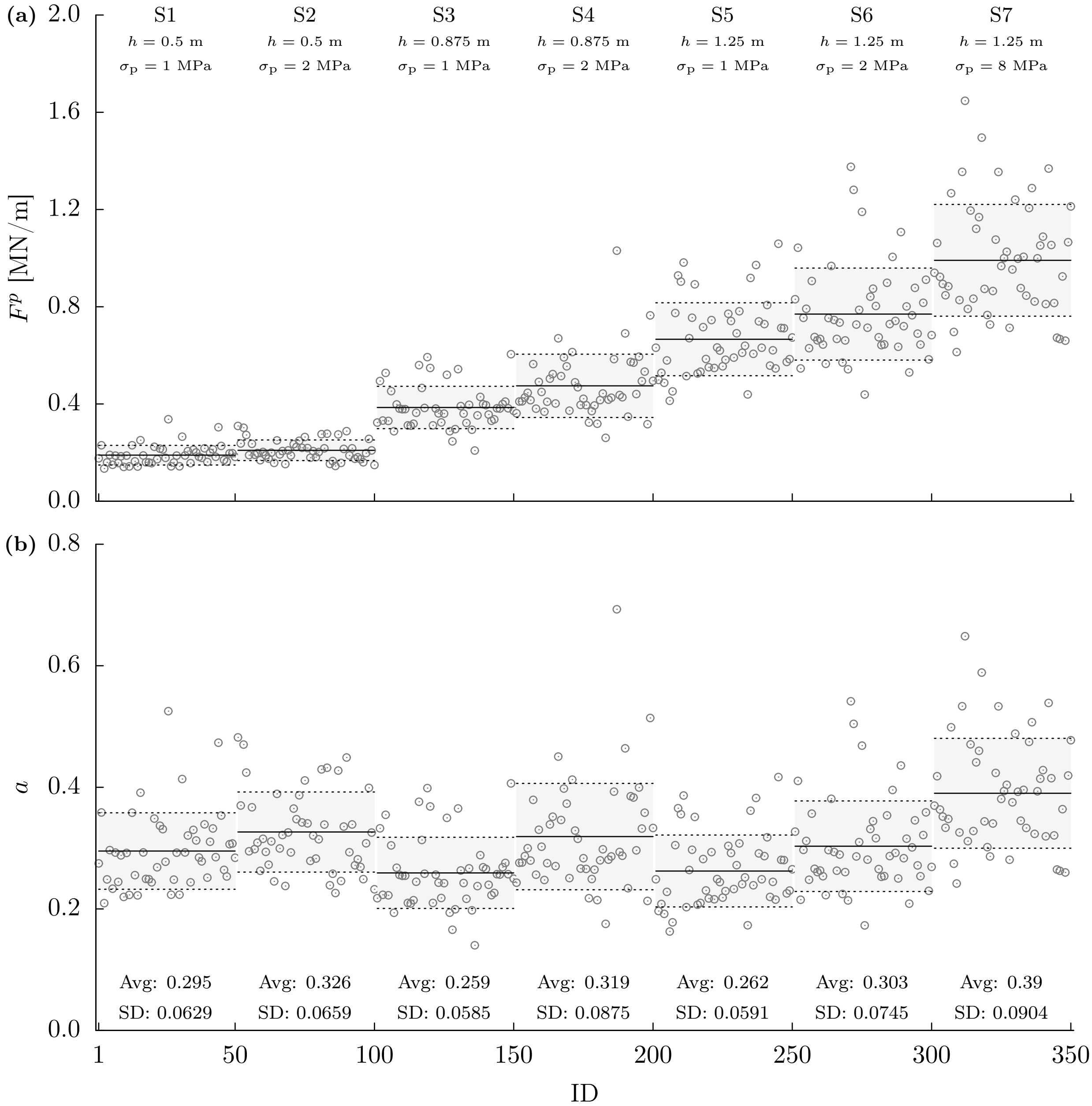

Figure 6: The values of (a) maximum peak ice loads F^p from all simulations in sets S1 ... S7 (Table 2) and (b) dimensionless a factors derived using the F^p data points (Equation 2). The graphs also give the mean values (Avg, solid lines) and standard deviations (SD, dashed lines) for the F^p and a data of each set. The mean a value 0.39 of set S7 was used in plotting Figure 8

that the values chosen for the maximum contact offset and number of contact interfaces, e_m and n, respectively, have only a very small effect on this observation.

4. Analysis and Discussion

This section first discusses how to extend the above-described limit load model into a numerical limit load algorithm. The algorithm enables detailed analysis of peak ice load events and shows potential in estimating the maximum peak ice load values and their distribution. The section also validates the model and the algorithm and discusses their applicability.

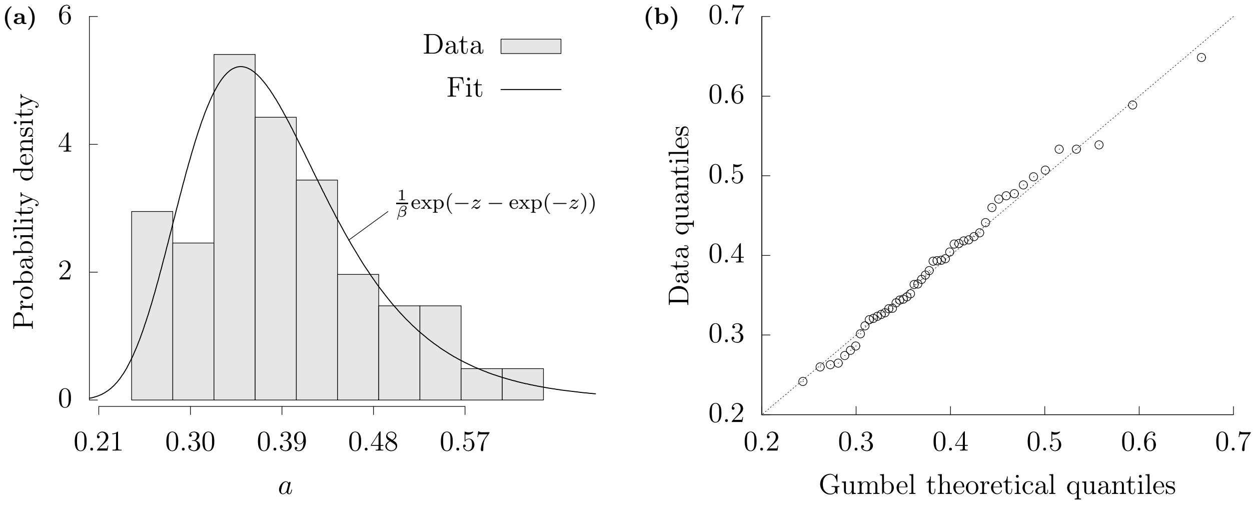

Figure 7: Distribution of a values related to set S7 with ice thickness h = 1.25 m and high crushing strength σ_p = 8 MPa: (a) histogram with fitted Gumbel (type I) extreme value distribution and (b) data quantiles (ordered a-values), plotted against the Gumbel theoretical quantiles. The Gumbel distribution with $z = (a - \mu)/\beta$ had estimated parameter values μ = 0.3495 (location) and β = 0.0705 (scale).

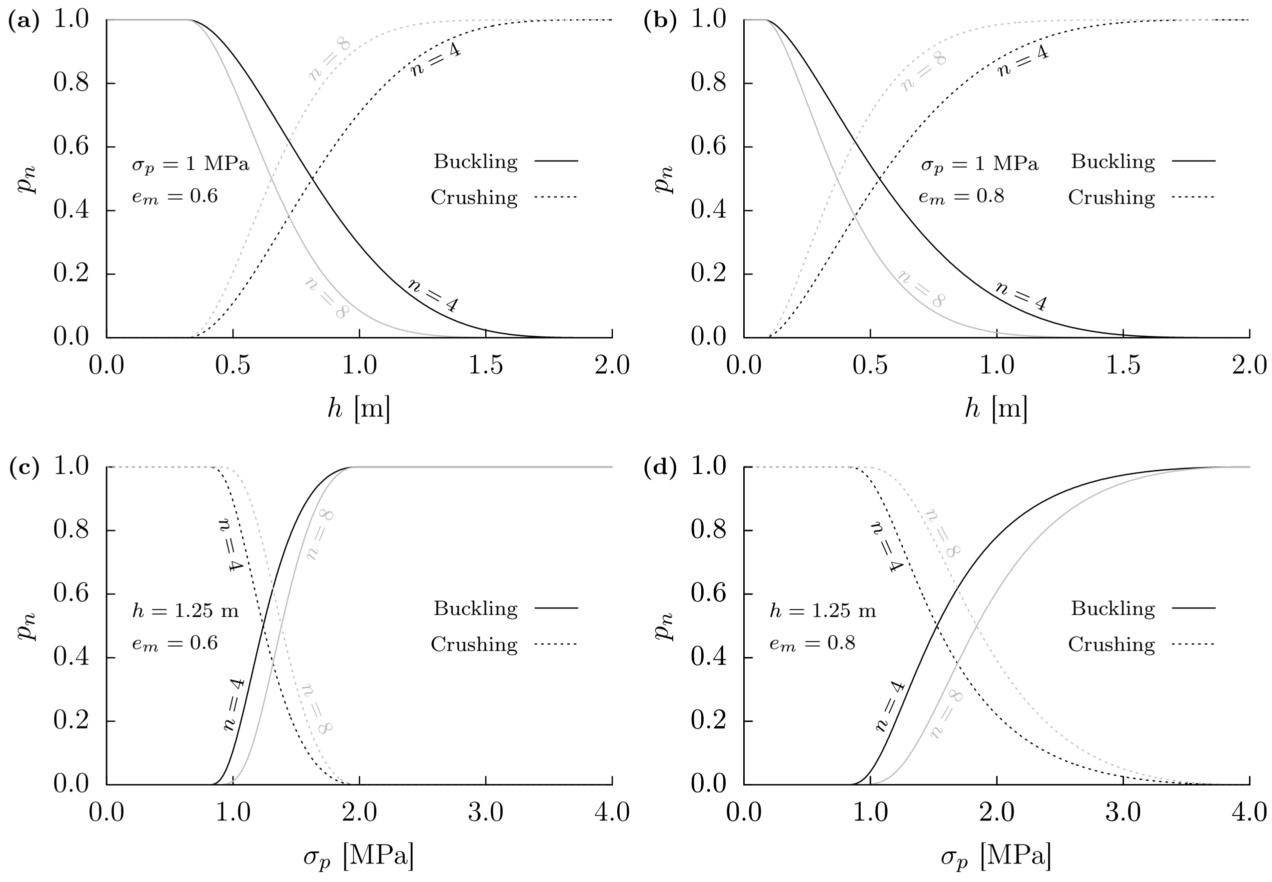

Figure 8: Probabilities for buckling and local crushing events, p_n(buckles) and p_n(crushes), respectively (Equations 10 and 11): (a) and (b) plotted against ice thickness h for crushing σ_p = 1 MPa and maximum contact offsets e_m = 0.6 and 0.8, respectively, and (c) and (d) as a function of σ_p for h = 1.25 m and e_m = 0.6 and 0.8, respectively. Parameter a had a fixed value of 0.39, which is the mean value of simulation set S7 (Figure 6b). Curves for two different number of contact interfaces, n, are shown in the figures.

4.1. Numerical limit load algorithm

The limit load model (Section 2.2) can be extended into a numerical limit load algorithm, which can be used to generate large amounts of virtual maximum peak ice load observations and related load

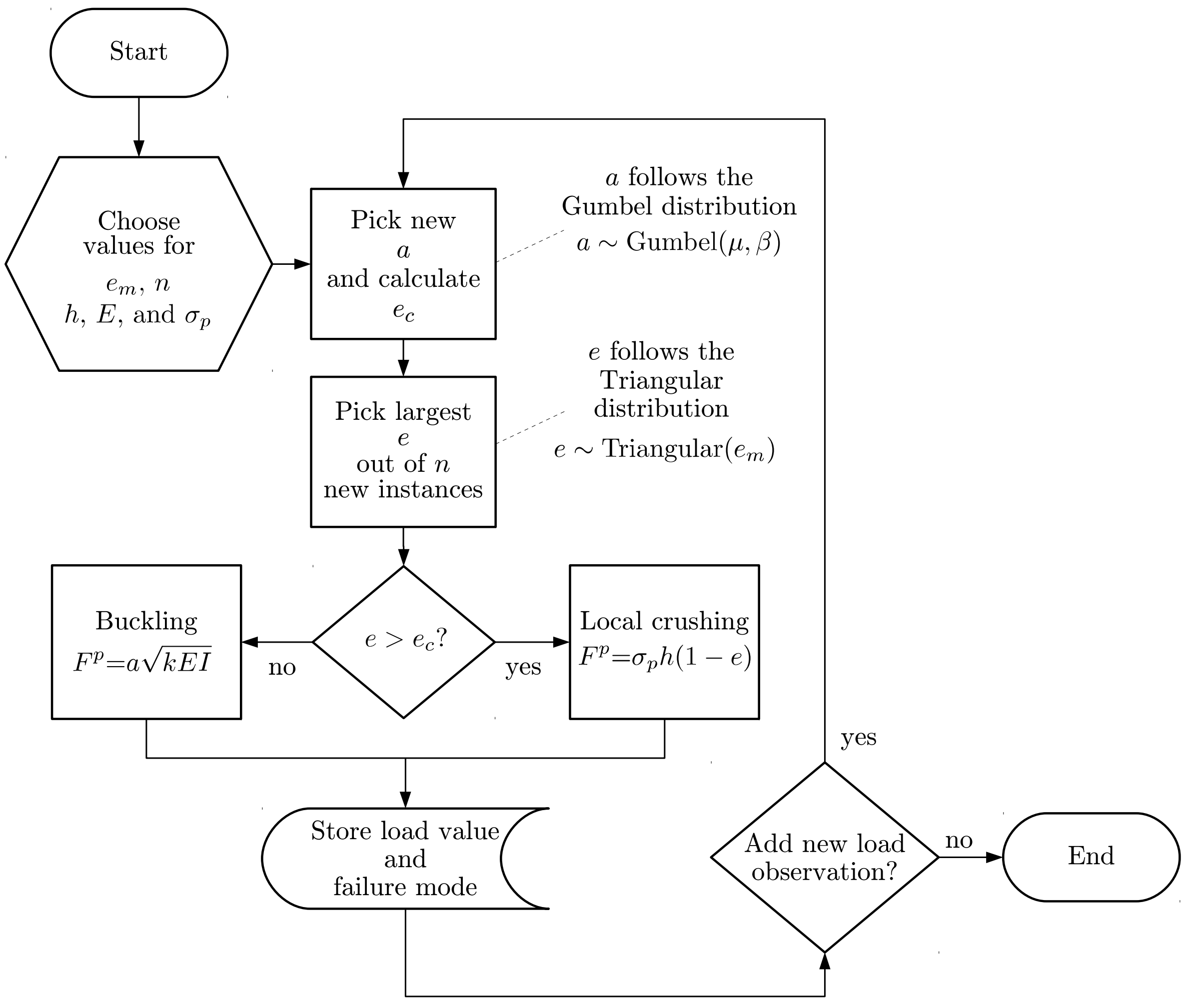

Figure 9: Flowchart describing the numerical limit load load algorithm, which yields virtual maximum peak ice load F^p observations. Table 1 describes the symbols shown in the flowchart. Equation 7 defines the triangular distribution required for e. Figure 7 gives the parameters of the Gumbel distribution for a factor.

distributions. The flowchart in Figure 9 describes the algorithm. As with the limit load model, it is based on the a-factor distribution and on the random non-dimensional contact offset e. (Examples of suitable distributions for e and a are, respectively, given by Figures 5 and 7.) In addition, the required input parameters are those needed to define the critical contact offset e_c (Equation 5), namely the water density ρ_w, ice thickness h, ice crushing strength σ_p, elastic modulus E, and gravitational acceleration g.

The flowchart in Figure 9 describes how to use the numerical limit load algorithm. For a floe-to-floe contact (number of contact interfaces $n = 1$), the algorithm yields one peak load observation by picking a random e and checking it against the critical contact offset e_c, solved by picking a random a value and substituting it into Equation 5. If $e \geq e_c$, the failure mode is local crushing and the algorithm yields a peak load value $F^p = \sigma_p h(1 - e)$ (Equation 6). On the other hand, if $e < e_c$, the failure mode is buckling and $F^p = a\sqrt{kEI}$. To achieve one peak load observation for a case having n contact interfaces, the algorithm picks n random values for e, and chooses the largest as it yields the lowest F^p. Multiple F_p observations can be made by repeating the procedure. We verified this approach by numerically reproducing the data described in Figure 8.

4.2. Simulated peak ice load events

We used the numerical limit load algorithm from the previous section to produce seven sets, A1…A7, of virtual F^p observations with the corresponding a values. Sets A1…A7 contained 100 observations each and they were parameterized, respectively, following the parameterization of the simulation sets of S1…S7. Tables 1 and 2 give the parameterization for sets S1…S7, while Figure 6 shows the F^p and a values from the FEM-DEM simulations. We created sets A1…A7 to verify the algorithm by comparing its results to those yielded by the FEM-DEM simulations. Here the values for the maximum contact offset and for the number of contact interfaces were fixed to $e_m = 0.8$ and $n = 4$, respectively, even if they varied throughout the FEM-DEM-simulated interaction process.

Figure 10 shows the a values calculated using the F^p observations originating from the numerical limit load algorithm. The algorithm yields virtual F^p data that fit well with the data from the FEM-DEM simulations. The mean values of a for sets A1…A7 are close, but slightly larger, to those of sets S1…S7, and the data show a similar dependency on σ_p than the data from the FEM-DEM simulations (see Figure 6b for comparison). We note that a one-to-one fit between the data sets would not be expected due to the stochasticity of the algorithm and the simulated ice-structure interaction process. We did not carry out any optimization for the parameters to obtain the best possible fit between data sets A1…A7 and S1…S7, which at least partially explains the tendency of the algorithm-produced values to be larger than the simulation-based ones.

The performance of the numerical limit load algorithm is further demonstrated in Figures 11a and b, which compare F^p data from selected FEM-DEM simulation sets to corresponding algorithm-produced F^p data sets. Figure 11a shows how the ice thickness h affects the results by showing the data related to sets A2, A4, and A6 (and corresponding sets S2, S4, and S6), which all had σ_p fixed to 2 MPa. Further, Figure 11b demonstrates the effect of σ_p by showing the data related to sets A5, A6, and A8 (and corresponding sets S5, S6, and S8), which had h fixed to 1.25 m. The figures show a similar non-linear trend for both the data from the simulations and the algorithm. The F^p values increase with h and σ_p, but the effect of σ_p becomes weaker with an increase in its value.

Figure 10 also shows the root cause of failure for all F^p observations generated by the algorithm. Triangular and square markers, respectively, indicate whether F^p was limited by a local crushing or buckling event. It is important to notice that there are more triangular markers for the data from sets A1, A3, and A5, which had relatively soft ice ($\sigma_p = 1$ MPa), than for the data from sets A2, A4, and A6, which had stronger ice ($\sigma_p = 2$ MPa). In the case of A7 ($\sigma_p = 8$ MPa), all F^p values were limited by buckling. Clearly, and as already suggested by Figure 8, stronger ice tends to buckle, and the maximum peak loads eventually become independent of the value of σ_p. This explains the increasing, but concave downward, trend in the F^p data in Figure 11b and, again, highlights the importance of describing the local phenomena; in other words, local crushing at the ice-ice contact interfaces when modeling ice-structure interaction.

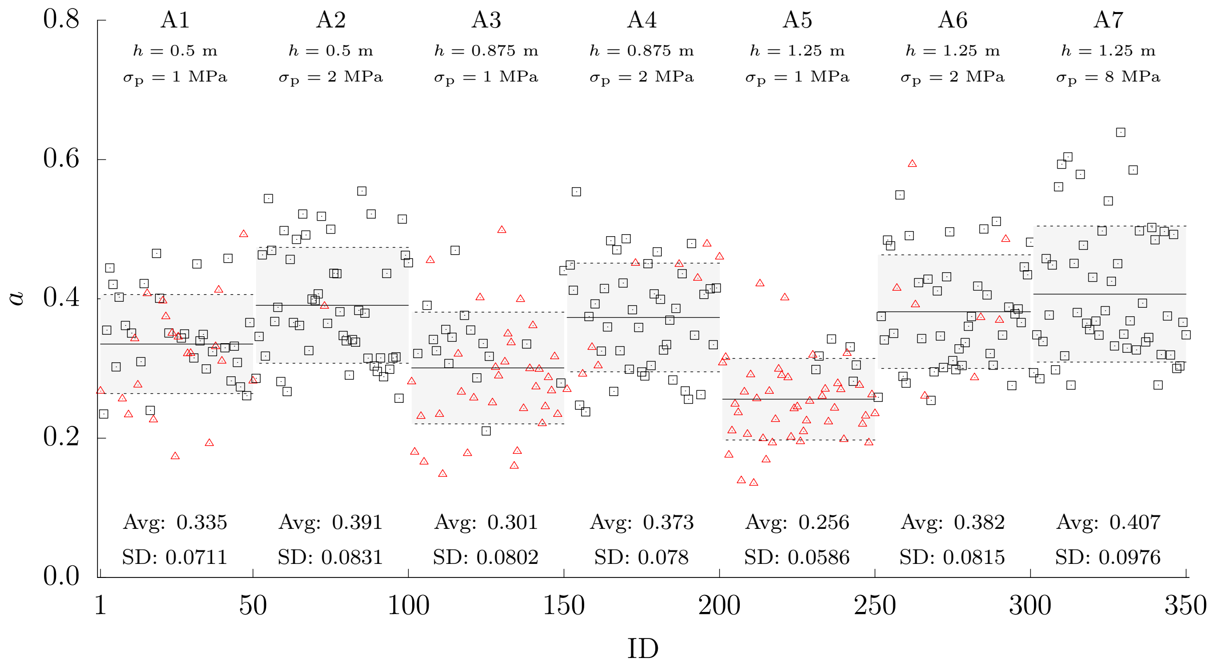

Figure 10: Dimensionless a factors (Equation 2) for the algorithm-produced maximum peak ice load F^p data sets A1...A7. Triangular (△) and square markers (□), respectively, indicate the local crushing and buckling events. The number of buckling events for sets A1...A7 were 30, 49, 17, 41, 6, 42, and 50, respectively (each set contained 50 observations). The graph also shows the mean values (solid lines) and standard deviations (dashed lines) for a data sets. Figure 6b shows similar figure for the FEM-DEM simulation data.

Another prominent feature of Figure 10 has to do with the markers indicating different failure modes, or load-limiting mechanisms, which are completely mixed for data sets A1...A6. This suggests that it is virtually impossible to distinguish between the different failure modes if the only data available from a peak ice load event is the load value. Interestingly, this notion would even apply for a hypothetical case in which all of the ice parameters were known. Instead of the load measurements, the detection of the failure mechanisms requires high-quality visual observations or other means to achieve detailed data on ice behavior. Unfortunately, ice failure can occur inside a mass of broken ice or under the snow cover in many real-world applications, which makes it extremely challenging to make direct observations related to the failure mechanisms. However, through careful analysis, ice load records may work as a source for detecting traces of them.

4.3. Validation of the numerical limit load algorithm

The previous section showed that the numerical limit load algorithm reproduces the peak ice load values, and the related parameter effects, in FEM-DEM simulations with good accuracy. Additionally, it is interesting to compare the algorithm-predicted peak ice load values to those measured in full-scale. Perhaps the best available data set for full-scale ice loads on a wide offshore structure, the Molikpaq caisson drilling platform, was that reported in Timco and Johnston [25]. According to them, the data originates from the observations made by Gulf Canada Resources, Esso Resources Canada, and Dome Petroleum (Canmar). Timco and Johnston [25] present distribution values for average ice pressure acting on the structure in cases of different ice failure modes based on the data. Furthermore, by using the means from the measured peak ice load distributions, they derived two

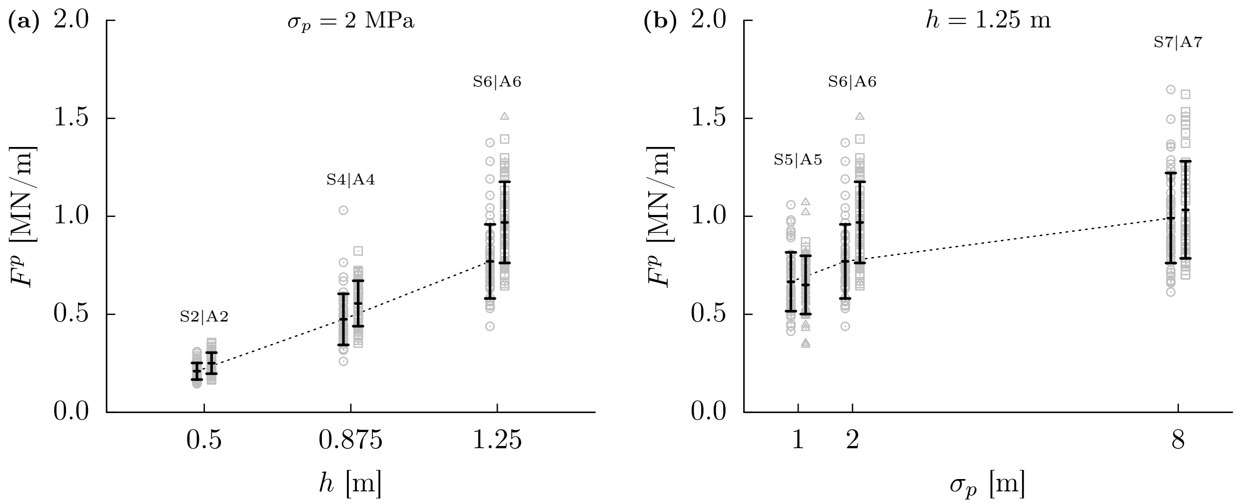

Figure 11: Maximum peak ice load F^p values from the FEM-DEM simulations (data sets S1…S7) and from the probabilistic limit load algorithm (A1…A7): F^p values plotted as a function of (a) the ice thickness h and (b) the plastic limit σ_p. Each parameter level has two adjacent sets of observations. Observations from the simulations and observations from the algorithm have a small offset for clarity. Error bars describe the mean value±one standard deviation of each underlying data set, with dashed lines connecting the mean values of the FEM-DEM data.

failure mode-dependent equations for the ice loads. They thus concluded that the highest ice loads were related to mixed-mode failure (in their case, a combination of local crushing, flexural failure and splitting), and to continuous ice crushing. The lowest loads came from the bending failure of ice.

Figures 12a and b compare the full-scale data from Timco and Johnston [25] with the data produced using the numerical limit load algorithm. Figure 12a shows 1000 algorithm-based peak ice load observations, produced by varying the ice thickness h and the plastic limit σ_p, with h ranging from 0.25 m to 1.5 m and σ_p from 1 MPa to 2 MPa (the physical maximum, or the ultimate line load in a hypothetical case of ice crushing through its whole thickness, would have been $F^p_{lim} = 2\,h$ [MN/m], where h is in meters). For each observation, we randomly picked unique h and σ_p values from a continuous uniform distribution. Figures 12b shows the normal cumulative probability distributions of the peak load observations produced by our algorithm and compares them to the full-scale peak load values. The parameters for plotting the three distributions for the full-scale data are given in Timco and Johnston [25].

The comparison presented in Figures 12a and b is clearly successful. Figure 12a shows that the algorithm-produced F^p observations, with only a few exceptions, fall between the continuous lines describing the load limits related to full-scale bending and crushing events and are, thus, within the expected range. All individual observations from the algorithm are considerably smaller than the physical limit F^p_{lim} shown by the dashed line. Further, the cumulative probability distributions for our data and for the data for mixed-mode failure presented in Timco and Johnston [25] are strikingly similar, as Figure 12b shows. We note that the algorithm-produced data in the figures here was generated using $n = 4$ contact interfaces and a thorough study on the effect of n is needed in the future.

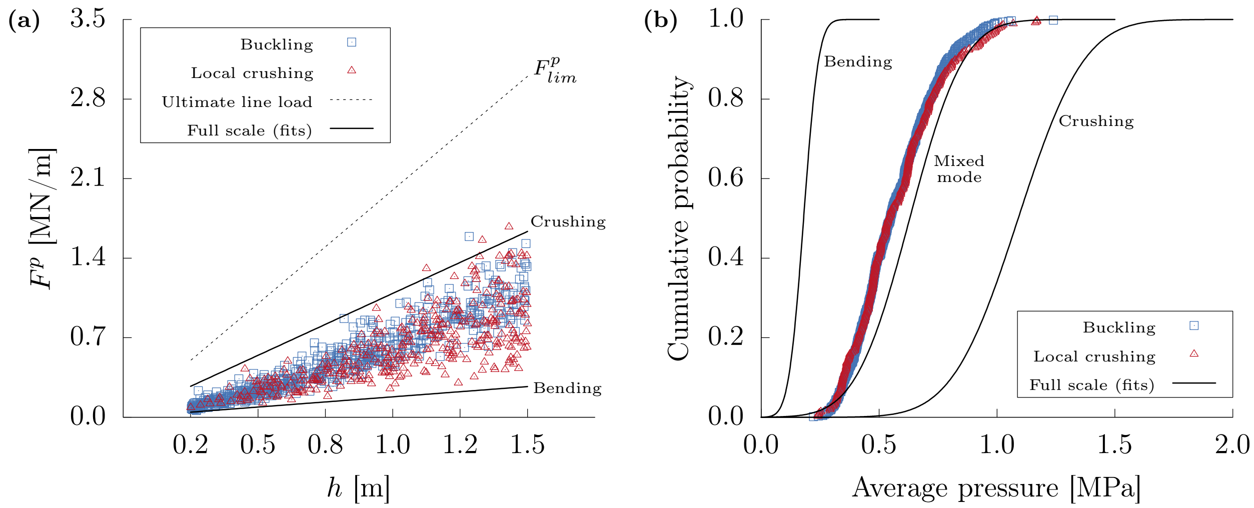

Figure 12: Comparison of numerical limit load algorithm and full-scale data: (a) 1000 algorithm-produced peak load observations (blue and red markers) and graphs for the loads from predictive equations for bending and crushing forces in full-scale [25] and (b) cumulative probabilities for the average pressure F^p/h. The physical limit F^p_{lim} for the loads (dashed line) is additionally shown in (a). The graph in (b) also shows cumulative probabilities for full-scale average pressures from bending, mixed-mode (in [25] local crushing, flexural failure, and splitting), and crushing events. Constants for the algorithm were $e_m = 0.8$ and $n = 4$.

4.4. Remarks on the limit load model and algorithm

The probabilistic limit load model and the related numerical limit load algorithm give new insights into the mechanics of ice loads. They can be applied to cases where the ice-structure interaction process exhibits a mixed-mode failure process, including force chain buckling and local ice crushing. This is not true for scenarios where ice does not transmit loads through force chains. Such scenarios could involve interaction processes with very warm ice or with soft model-scale ice in laboratory-scale experiments (given that the buckling occurs in a full-scale interaction process, this type of experiment would not then exhibit all significant features of a full-scale process). The assumption of 2D ice loading scenario limits the applicability of the model, and future work is required to extend it to a 3D scenario. The ice in a 2D scenario does not clear around the structure, but keeps on piling up (and down) in front of the structure. The results should anyhow, with fair accuracy, apply to wide structures in deep waters. We acknowledge, that even for this case, more measurements on the effect of non-simultaneous failure on global and local ice loads would be useful to fully justify the applicability of our model.

Future parametric studies using the limit load model are required. It is challenging to choose values for ice loading process-dependent parameters, the maximum contact offset and the number of contact interfaces, e_m and n, respectively. It is clear that e_m must not have a value very close to one, as then our model would yield very low peak load predictions (it is not of engineering interest to study ice loading processes yielding very low peak ice load values). Related to this, choosing the distribution for e should be also addressed. For example, a uniform distribution would lead to lower peak loads than the triangular one as the expected value of e would increase. On the other hand, n will attain several different values during any realistic ice-structure interaction process, whereas it is on the level of the whole process that the model is intended to work. Picking a unique value for n is thus impossible, even if its maximum value must be limited due to the highly compressed force-chains having finite lengths, which may depend on, for example, the amount of rubble in front of the structure. It is worth noting, however, that the model yields important findings independent of e_m and n, since for example, the lower limit needed for the crushing strength of ice of a given ice thickness to exhibit a mixed-mode failure process does not depend on them (Figure 8). We also note that we did not yet do any parameter optimization, but still obtained reasonable results using our model and algorithm.

The limit load model and the numerical limit load algorithm are both rather simple tools for the analysis of peak ice load events, and they show the potential for predicting maximum peak ice load values on wide, inclined structures. We are unaware of any other approaches that have such a solid basis in the mechanics of ice behavior, while simultaneously accounting for the statistics of the loads. This is the strength of the algorithm: Its mechanical basis may allow for more reliable analysis and load predictions than empirical ice load models or simple analytical calculation models [22, 66], which do not account for the effects of the complex failure process. The predictive power of the model was demonstrated by our successful comparison of the algorithm-produced and full-scale data. This comparison gives confidence to the ice load analysis based on the limit load model and to the predictive power of the algorithm.

5. Conclusions

This paper introduced a probabilistic limit load model for the analysis of peak ice load events on an inclined offshore structure during an ice-structure interaction process. The model is based on simple mechanical principles and it accounts for a mixed-mode ice failure process that includes ice buckling and local crushing. The paper also presented a numerical limit load algorithm, which is an extension of the probabilistic limit load model and can be used to generate a very large number of stochastic peak ice load observations. Some of the most important findings presented above are as follows:

- The probabilistic limit load model and algorithm explain the effect of ice thickness and crushing strength of ice on peak ice loads in FEM-DEM simulations (Section 4.2). They also produce peak ice load values that compare well with the full-scale data (Section 4.3).
- Local ice crushing at ice-block-to-ice-block contact interfaces is an important factor affecting the maximum peak ice load events in an ice-structure interaction process (Section 3.2). This highlights the importance of accounting for local crushing in the modeling.
- Algorithm-produced peak load data sets (Figure 10) are collections of overlapping load observations related to both buckling and local crushing. It may, thus, be impossible to detect the root cause of ice failure without observations focusing on this in a real-world experiment.

Analyzing the peak ice load events in an ice-structure interaction process is challenging due to the complex ice failure process. We believe the probabilistic limit load model and algorithm have the potential to offer new insights for this type of analysis, which in turn will lead to improved and safer design of offshore structures.

Acknowledgments

We are grateful for the financial support from the Academy of Finland research projects (309830) Ice Block Breakage: Experiments and Simulations (ICEBES) and (268829) Discrete Numerical Simulation and Statistical Analysis of the Failure Process of a Non-Homogenous Ice Sheet Against an Offshore Structure (DICE). We wish to acknowledge the support from the Research Council of Norway through the Centre for Research-based Innovation SAMCoT and the support from all SAMCoT partners. We also wish to thank the two anonymous reviewers whose insightful comments and suggestions helped us to improve the manuscript.

Appendix A: Buckling model

Figure 13 shows the buckling model extended in this paper in its unloaded and loaded states. The model considers a rigid system consisting of an ice floe, or a few ice floes compressed together, having total length L_f resting on an elastic foundation having a modulus of k and discrete springs having spring constants K_1 and K_2. The modulus k of the elastic foundation was $k = \rho_w g$, where ρ_w is the mass density of the water and g is the gravitational acceleration. The axial compressive load P results from an interaction with an adjacent ice floe or from an interaction with an ice rubble pile. The critical buckling load of the system is [6]

$$P_{cr} = \frac{k^2 L_f^3 + 4k(K_1 + K_2)L_f^2 + 12K_1K_2L_f}{12(kL_f + K_1 + K_2)} \tag{13}$$

Spring constants $K_1 = C_1kL_c - C_2P/L_c$ and $K_2 = C_3kL_c - C_4P/L_c$, where $L_c = \sqrt[4]{4EI/k}$ is the characteristic length [67], account for different boundary conditions depending on the choice of values for positive constants $C_1 \ldots C_4$. By plugging these spring constants into Equation 13, and further by substitutions $L_f = \chi L_c$ and $P = P_{cr}$, the critical load may be written concisely as

$$P_{cr} = a\sqrt{kEI}, \tag{14}$$

where $a = a(C_1, C_2, C_3, C_4, \chi)$ is a dimensionless buckling load factor and χ is a dimensionless buckling length factor. Equation 14 is valid, irrespective of the choice of values for $C_1 \ldots C_4$, and Table 3 demonstrates four different buckling modes associated with different combinations of them. These buckling modes were presented in Ranta et al. [6]. In modes 1 and 2, the system of length L_f buckles alone, whereas in modes 3 and 4 the system of length L_f is affected on the left-hand side by an intact semi-infinite ice sheet. Buckling in the ice load models by Coon [10] and McKenna et al. [11] occurred in mode 1. Mode 2 was used by Carter [12] to describe level ice failure against a vertical structure. The applicability of different buckling modes in the analysis of peak ice loads on inclined structures was discussed in detail by Ranta [6].

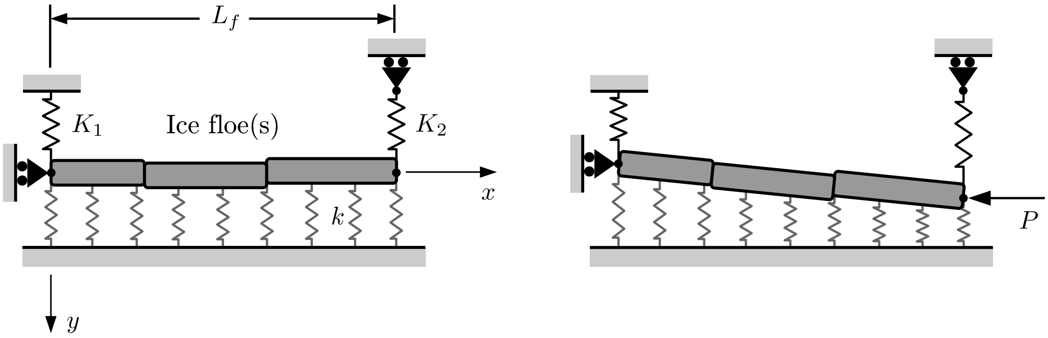

Figure 13: The buckling model in its initial (left) and buckled (right) states. The model consists of an ice floe or several ice floes having total length L_f resting on an elastic foundation with modulus k presenting water. Springs with spring constants K_1 and K_2 modeled the boundary conditions for the buckling modes shown in Table 3. Compressive force P is due to the other floes or the structure.

Table 3: Four buckling modes considered in our study, together with the corresponding spring constants K_1 and K_2 (Figure 13). The buckling load is $P = a\sqrt{kEI}$, where $a = a(\chi)$ is a dimensionless multiplier that has a mode-dependent expression. Factor χ gives the buckling length L_f as described in the text.

Mode	C_1	C_2	C_3	C_4	$a(\chi)$	Mode shape $\leftarrow L_f \rightarrow$
1	0	0	0	0	$\dfrac{\chi^2}{6}$	
2	∞	0	0	0	$\dfrac{2\chi^2}{3}$	
3	$\dfrac{1}{2}$	$\dfrac{3}{4}$	∞	0	$\dfrac{12\chi + 8\chi^2}{9\chi + 12}$	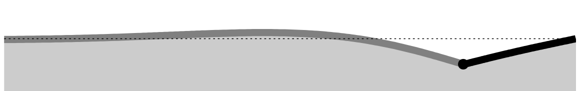
4	1	$\dfrac{1}{2}$	∞	0	$\dfrac{12\chi + 4\chi^2}{3\chi + 6}$	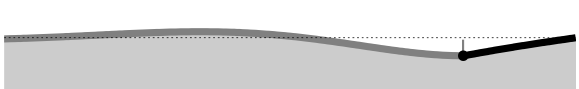

References

[1] Sanderson, T. Ice Mechanics, Risks to Offshore Structures. Graham & Trotman Inc. Kluwer Academic Publishers Group; 1988.

[2] Daley, C., Tuhkuri, J., Riska, K. The role of discrete failures in local ice loads. Cold Regions Science and Technology 1998;27(3):197–211.

[3] Jordaan, I. Mechanics of ice-structure interaction. Engineering Fracture Mechanics 2001;68:1923–1960.

[4] Cundall, P., Strack, O. A discrete numerical model for granular assemblies. Géotechnique 1979;29(1):47–65.

[5] Munjiza, A. The combined finite-discrete element method. John Wiley & Sons Ltd., Chichester, England; 2004.

[6] Ranta, J., Polojärvi, A., Tuhkuri, J. Limit mechanisms for ice loads on inclined structures: Buckling. Cold Regions Science and Technology 2018;147:34–44.

[7] Peters, J., Muthuswamy, M., Wibowo, J., Tordesillas, A. Characterization of force chains in granular material. Physical Review E - Statistical, Nonlinear, and Soft Matter Physics 2005;72(4).

[8] Tordesillas, A., Walker, D.M., Lin, Q. Force cycles and force chains. Physical Review E - Statistical, Nonlinear, and Soft Matter Physics 2010;81:011302.

[9] Paavilainen, J., Tuhkuri, J. Pressure distributions and force chains during simulated ice rubbling against sloped structures. Cold Regions Science and Technology 2013;85:157–174.

[10] Coon, M. Mechanical behavior of compacted Arctic ice floes. Journal of Petroleum Technology 1974;26:466–470.

[11] McKenna, R., Spencer, D., Lau, M., Walker, D., Crocker, G. Modelling the forces exerted by pack ice consisting of small floes. In: Proceedings of OMAE'97, 16th International Conference on Offshore Mechanics and Arctic Engineering; vol. IV. Yokohama, Japan; 1997, p. 329–338.

[12] Carter, D., Sodhi, D., Stander, E., Caron, O., Quach, T. Ice thrust in reservoirs. Journal of Cold Regions Engineering 1998;12(4):169–183.

[13] Ranta, J., Tuhkuri, J., Polojärvi, A. The statistical analysis of peak ice loads in a simulated ice-structure interaction process. Cold Regions Science and Technology 2017;133:46–55.

[14] Cundall, P., Drescher, A., Strack, O. Numerical experiments on granular assemblies; measurements and observations. In: Proceedings of lUTAM Symposium on Deformation and Failure of Granular Materials. Delft, Netherlands; 1982, p. 355–370.

[15] Cundall, P., Strack, O. Modeling of Microscopic Mechanisms in Granular Material. Elsevier Science Publishers B.V; 1983, p. 137–149.

[16] Kerr, A.D. On the determination of horizontal forces a floating ice plate exerts on a structure. Journal of Glaciology 1978;20(82):123–134.

[17] Sodhi, D. Buckling analysis of wedge-shaped floating ice sheets. In: Proceedings of the 5th International Conference on Port and Ocean Engineering under Arctic Conditions, POAC'79. Trondheim, Norway; 1979.

[18] Sodhi, D., Haynes, F., Kato, K., Hirayama, K. Experimental determination of the buckling loads of floating ice sheets. Annals of Glaciology 1983;4:260–265.

[19] Kärnä, T., Jochmann, P. Field observations on ice failure modes. In: Proceedings of the 17th International Conference on Port and Ocean Engineering under Arctic Conditions, POAC'03. Trondheim, Norway; 2003.

[20] Hendrikse, H., Metrikine, A. Ice-induced vibrations and ice buckling. Cold Regions Science and Technology 2016;131:129–141.

[21] Croasdale, K. Ice forces on fixed, rigid structures. Special Report 80–26; Cold Regions Research and Engineering Laboratory; 1980.

[22] Croasdale, K., Cammaert, A., Metge, M. A method for the calculation of sheet ice loads on sloping structures. In: Proceedings of the 12th International Symposium on Ice IAHR. Trondheim, Norway; 1994, p. 874–885.

[23] Lu, W., Lubbad, R., Serré, N., Løset, S. A theoretical model investigation of ice and wide sloping structure interactions. In: Proceedings of the 22nd International Conference on Port and Ocean Engineering under Arctic Conditions, POAC'13 (electronic publication). Espoo, Finland; 2013.

[24] Lu, W., Lubbad, R., Høyland, K., Løset, S. Physical model and theoretical model study of level ice and wide sloping structure interactions. Cold Regions Science and Technology 2014;101:40–72.

[25] Timco, G., Johnston, M. Ice loads on the caisson structures in the canadian beaufort sea. Cold Regions Science and Technology 2004;38(2–3):185–209.

[26] Munjiza, A., Owen, D., Bićanić, N. A combined finite-discrete element method in transient dynamics of fracturing solids. 1995;12:145–174.

[27] Paavilainen, J., Tuhkuri, J., Polojärvi, A. 2D combined finite–discrete element method to model multi-fracture of beam structures. Engineering Computations 2009;26(6):578–598.

[28] Paavilainen, J., Tuhkuri, J., Polojärvi, A. 2D numerical simulations of ice rubble formation process against an inclined structure. Cold Regions Science and Technology 2011;68(1–2):20–34.

[29] Paavilainen, J., Tuhkuri, J. Parameter effects on simulated ice rubbling forces on a wide sloping structure. Cold Regions Science and Technology 2012;81:1–10.

[30] Saarinen, S. Description of the pile-up process of an ice sheet against an inclined plate. Master's thesis; Helsinki University of Technology; 2000.

[31] Williams, R., Mustoe, G., Worgan, K. Force transfer and behavior of rubble piles. In: Proceedings of the 8th IAHR International Symposium on Ice. Iowa city, IA, USA; 1986.

[32] Hopkins, M., Hibler III, W.D. On the shear strength of geophysical scale ice rubble. Cold Regions Science and Technology 1991;19(2):201–212.

[33] Hopkins, M. Numerical simulation of systems of multitudinous polygonal blocks. Tech. Rep. 92–22; Cold Regions Research and Engineering Laboratory, CRREL; 1992. 69 p.

[34] Hopkins, M. Four stages of pressure ridging. Journal of Geophysical Research 1998;103(C10):21,883–21,891.

[35] Hopkins, M., Tuhkuri, J., Lensu, M. Rafting and ridging of thin ice sheets. Journal of Geophysical Research 1999;104(C6):13605–13613.

[36] Barker, A., Croasdale, K. Numerical modelling of ice interaction with rubble mound berms in the Caspian Sea. In: Proceedings of the 17th IAHR International Symposium on Ice, Saint Petersburg, Russia. 2004, p. 257–264.

[37] Liferov, P. Ice rubble behaviour and strength: Part II. Modelling. Cold Regions Science and Technology 2005;41(2):153–163.

[38] Tuhkuri, J., Polojärvi, A. Effect of particle shape in 2D ridge keel deformation simulations. In: Proceedings of the 18th International Conference on Port and Ocean Engineering under Arctic Conditions, POAC'05; vol. 2. Potsdam, New York, USA; 2005, p. 939–948.

[39] Polojärvi, A., Tuhkuri, J. 3D discrete numerical modelling of ridge keel punch through tests. Cold Regions Science and Technology 2009;56(1):18–29.

[40] Polojärvi, A., Tuhkuri, J. On modeling cohesive ridge keel punch through tests with a combined finite-discrete element method. Cold Regions Science and Technology 2013;85:191–205.

[41] Polojärvi, A., Tuhkuri, J. Discontinuum modelling in interpretation of punch through tests on partly consolidated sea ice rubble. In: DEM6, 6th International Conference on Discrete Element Methods (electronic publication). August 5-6, Golden, Colorado, USA; 2013.

[42] Konuk, I., Gürtner, A., Yu, S. Study of dynamic ice and cylindrical structure interaction by the cohesive element method. In: Proceedings of the 20th International Conference on Port and Ocean Engineering under Arctic Conditions, POAC'09 (electronic publication). Luleå, Sweden; 2009.

[43] Polojärvi, A., Tuhkuri, J., Korkalo, O. Comparison and analysis of experimental and virtual laboratory scale punch through tests. Cold Regions Science and Technology 2012;81:11–25.

[44] Polojärvi, A., Pustogvar, A., Tuhkuri, J. DEM simulations of direct shear box experiments of ice rubble: Force chains and peak loads. Cold Regions Science and Technology 2015;(116):12–23.

[45] Metrikin, I., Løset, S. Nonsmooth 3D discrete element simulation of a drillship in discontinuous ice. In: Proceedings of the 22nd International Conference on Port and Ocean Engineering under Arctic Conditions, POAC'13 (electronic publication). Espoo, Finland; 2013.

[46] Metrikin, I., Gürtner, A., Bonnemaire, B., Tan, X., Fredriksen, A., Sapelnikov, D. SIBIS: a numerical environment for simulating offshore operations in discontinuous ice. In: Proceedings of the 23rd International Conference on Port and Ocean Engineering under Arctic Conditions, POAC'15 (electronic publication). in Trondheim, Norway; 2015.

[47] Shunying, J., Shaocheng, D., Shewen, L. Analysis of ice load on conical structure with discrete element method. Engineering Computations 2015;32(4):1121–1134.

[48] van den Berg, M., Lubbad, R., Løset, S. An implicit time-stepping scheme and an improved contact model for ice-structure interaction simulations. Cold Regions Science and Technology 2018;155:193–213.

[49] Tuhkuri, J., Polojärvi, A. A review of discrete element simulation of ice-structure interaction. Philosophical Transactions of the Royal Society A: Mathematical, Physical and Engineering Sciences 2018;376(2129).

[50] Schreyer, H., Sulsky, D., Munday, L., Coon, M., Kwok, R. Elastic-decohesive constitutive model for sea ice. Journal of Geophysical Research: Oceans 2006;111(11).

[51] Hillerborg, A., Modéer, M., Petersson, P.E. Analysis of crack formation and crack growth in concrete by means of fracture mechanics and finite elements. Cement and Concrete Research 1976;6:773–82.

[52] Dempsey, J., Adamson, R., Mulmule, S. Scale effects on the in-situ tensile strength and fracture of ice. Part II: first-year sea ice at resolute, N.W.T. International Journal of Fracture 1999;95:347–366.

[53] Timco, G., Weeks, W. A review of the engineering properties of sea ice. Cold Regions Science and Technology 2010;60(2):107–129.

[54] Ranta, J., Polojärvi, A., Tuhkuri, J. Sources of stochasticity in ice-structure interaction process. In: Proceedings of the 24th International Conference on Port and Ocean Engineering under Arctic Conditions, POAC'17 (electronic publication). Busan, Korea; 2017.

[55] Ranta, J., Polojärvi, A., Tuhkuri, J. Scatter and error estimates in ice loads—Results from virtual experiments. Cold Regions Science and Technology 2018;148:1–12.

[56] Ranta, J., Polojärvi, A., Tuhkuri, J. Ice loads on inclined marine structures—Virtual experiments on ice failure process evolution. Marine Structures 2018;57:72–86.

[57] Kheisin, D., Popov, Y. Ice navigation qualities of ships. Tech. Rep.; Cold Regions Research and Engineering Laboratory (CRREL); 1973.

[58] Kujala, P. On the statistics of ice loads on ship hull in the Baltic. Acta Polytechnica Scandinavica, Mechanical Engineering Series No 116, Helsinki 1994.

[59] Brown, T., Jordaan, I., Croasdale, K. A probabilistic approach to analysis of ice loads for the confederation bridge. Canadian Journal of Civil Engineering 2001;28(562–573).

[60] Brown, T., Elseify, M. Ice ridges interaction with confederation bridge piers, results of detailed video and sonar data analysis. In: Proceedings of the 18th International Symposium on Ice, IAHR. 2006.

[61] Fransson, L., Lunqvist, J.E. A statistical approach to extreme ice loads on lighthouse norströmsgrund. In: Proceedings of OMAE'06, 25th International Conference On Offshore Mechanics and Artcic Engineering. Hamburg, Germany; 2006.

[62] Kärnä, T., Qu, Y., Yue, Q. An extreme value analysis of local ice pressures. In: ICETECH-06 Proceedings of the International Conference and Exhibition on Performance of Ships and Structures in Ice. Alberta, Canada; 2006.

[63] Qu, Y., Yue, Q., Bi, X., Kärnä, T. A random ice force model for narrow conical structures. Cold Regions Science and Technology 2006;45:148–157.

[64] Kujala, P., Suominen, M., Riska, K. Statistics of ice loads measured on mt uikku in the baltic. In: Proceedings of the 20th International Conference on Port and Ocean Engineering under Arctic Conditions, POAC'09 (electronic publication). Luleå, Sweden; 2009.

[65] Suyuthi, A., Leira, B., Riska, K. Statistics of local ice load peaks on ship hulls. Structural Safety 2013;40:1–10.

[66] Määttänen, M. Ice sheet failure against an inclined wall. In: Proceedings of the 8th IAHR International Symposium on Ice. Iowa City, U.S.A.; 1986, p. 149–158.

[67] Hetényi, M. Beams on elastic foundation: Theory with applications in the fields of civil and mechanical engineering. Ann Arbor: The University of Michigan Press; 1979.